Fast Magnetic Field Approximation Method for Simulation of Coaxial Magnetic Gears using AI

Huihuan Wu, Shuangxia Niu*, Yunpeng Zhang, Xing Zhao, and Weinong Fu

***Abstract*—Artificial intelligence (AI) and Deep Learning (DL) have been widely used in recent years to explore the possibility of accelerating computation. However, it has very few applications in magnetic field calculation. This article employs a conditional generative adversarial network (cGAN) to approximate the magnetic field of a coaxial magnetic gear (CMG) and calculate the magnetic torque through post-processing. The working principle of magnetic field approximation using cGAN and the training process is introduced in this study. We adopted conditional image-to-image translation technology in cGAN and compared different loss functions and residual structures combinations. Then, we found the best combination, which can accelerate convergence, reduce errors, and improve the generator's performance. Numerical experiments have verified the effectiveness of the proposed cGAN, and the average numerical error can be as small as 1%. At the same time, its speedup ratio is as high as 200 compared to the finite element method (FEM).**

***Index Terms*—Deep learning, FEM, GAN, magnetic gear, neural network**

I. Introduction

MAGNETIC gears have attracted much attention due to the advantages of free-of-contact, inherent overload capability, silent operation, and high reliability compared with mechanical gears [1], [2]. The coaxial magnetic gear (CMG), which comprises coaxial inner and outer rotors on the two sides of ferromagnetic segments, realizes a better utilization of PMs and transmits significantly higher torque density compared with other types of MGs [3], [4]. Therefore, CMGs have been employed in critical environments to meet the high requirement and harsh working conditions. For example, high-efficiency and high-performance magnetic gears have been used in electric vehicles (EVs) [5], electricity propelled ships [6], [7], and electric aircraft [8]–[10].

Many methods are developed to improve the performance of magnetic gears, such as the analytical method [2], [11], equivalent magnetic circuit method [12], finite element (FE) method, and so on [13]–[15]. However, the current calculation methods have some shortcomings. The FE method is an accurate tool for simulation but the operations when the FE simulation, which involves meshing, global matrix assembly, and matrix inversion, is exceedingly extremely time-consuming. On the contrary, the analytical method requires few computation resources, but the generalization ability is limited.

In recent years, with the development of AI technology, the AI-based field approximation offers an alternative approach to improving magnetic gears' performance. AI is commonly used for classification and regression, especially in computational visual processing. It has been gradually used for complex data fitting with the continuous development of data-driven methods [16]–[21]. Both supervised and unsupervised learning approaches have been applied to magnetic field approximation [14], [22]–[25].

So far, a series of AI and DL concepts have been proposed, including deep neural networks with fully connected networks (FCN), convolutional networks (CNN), and generative adversarial networks (GAN) [14], [26], [27].

These preliminary results show that deep neural networks can learn the relationship between structural geometry and magnetic field distribution. Still, they also highlight critical challenges to the approach [28]. One challenge is that the computation cost of creating the training data set itself can be huge. A simple, fully connected dense network described by a few geometric parameters requires tens of thousands to hundreds of thousands of samples for training. Promising results are derived with these networks, but the training of these models relies on sufficient data, the generation of which is extremely time-consuming. In this regard, GAN-based technology can reduce the number of training samples and obtain better generalization capabilities among many neural networks [21].

This paper introduces a new concept for magnetic performance evaluation by approximating magnetic fields directly from a conditional GAN. Our approach can evaluate the CMG performance, such as air gap flux density and transmission torque, with modest computational cost in terms of novel CMG design. Unlike the analytical method, the model proposed in this paper could derive the entire magnetic field distribution in the design space, which is beneficial for further analysis. In addition, we utilize a physics-based loss function to ensure that the network training is directly performance parameters.

Huihuan Wu is with the Department of Electrical Engineering, The Hong Kong Polytechnic University, Hong Kong (email: hh.wu@connect.polyu.hk.)

Shuangxia Niu is with the Department of Electrical Engineering, The Hong Kong Polytechnic University, Hong Kong (email: eesxniu@polyu.edu.hk).

Xing Zhao is with the School of Physics, Engineering and Technology, University of York, United Kingdom (email xing.zhao@york.ac.uk)

Yunpeng Zhang is with the School of Mechatronic Engineering and Automation, Shanghai University, Shanghai, CN (email: zyp_19@shu.edu.cn).

Weinong Fu is with the Shenzhen Institutes of Advanced Technology, Chinese Academy of Sciences, Shenzhen, CN (email: wn.fu@siat.ac.cn).

Corresponding author: Shuangxia Niu.

This paper is divided into seven parts. Section II introduces the general knowledge about magnetic gear and the torque calculation method. Section III deals with the preliminary background and concept of generative adversarial networks (GANs). Section IV is concerned with the methodology used for this study. This section introduces the working principle, the architecture of the proposed network, the training process, the PM representation method, and neural network configurations. Section V introduces the key parameters that influence the neural network's performance. Section VI demonstrates the preliminary results obtained from the proposed network. The conclusion is drawn in Section VII.

II. Technical Preliminaries

This section formulates the magnetic gear working principle and the torque calculation using the Maxwell stress tensor method in the polar coordinate system.

A. Magnetic Gears

Since Magnetic gears utilize the energy exchange between magnetic field energy and mechanical energy, they have many advantages compared with traditional mechanical gears.

The first high-performance magnetic gear was proposed in 2001 [29]. The main components of this CMG are shown in Fig. 1.

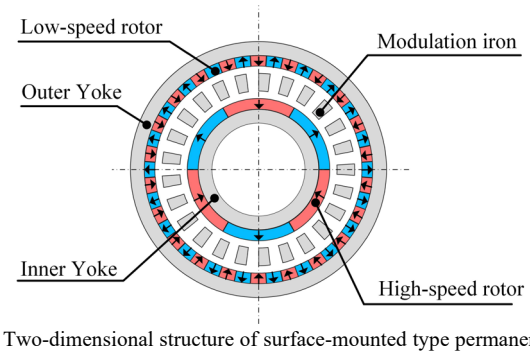

Fig. 1. Two-dimensional structure of surface-mounted type permanent magnet (PM) coaxial magnetic gear.

The operation of CMG is based on modulating the magnetic field produced by the rotating magnetic poles of the high-speed rotor in the iron poles of the stationary part; meanwhile, the low-speed rotor will be driven in the opposite direction by the magnetic field modulated in the modulation iron. It has been shown that the highest torque transmission is obtained with the following equality [1]:

$$p_{out} = N_s - p_{in} \tag{1}$$

where p_{in} is the number of poles pair for the inner (high-speed) rotor, N_s is the number of modulation iron segments, and p_{out} is the number of outer (low speed) rotor, respectively.

The correlation between the output (ω_{out}) and input (ω_{in}) speed and the gear ratio (gr) are:

$$\omega_{out} = gr \times \omega_{in} \tag{2}$$

$$gr = \frac{\omega_{out}}{\omega_{in}} = -\frac{p_{in}}{p_{out}} \tag{3}$$

Furthermore, an optimal combination exists among p_{out}, p_{in} and N_s, which can significantly reduce the torque ripple when CMG is in operation [30]. This relationship can be defined by a coefficient k_r.

$$k_r = \frac{2p_{in} \times N_s}{LCM(2p_{in}, N_s)} \tag{4}$$

where LCM indicates the 'least common multiple' between p_{in} and N_s. The minimal ripple exists when the coefficient k_r reaching to 1.

B. Magnetic performance of CMGs

1) Air Gap Flux Density

Air-gap flux density is one of the most critical parameters to optimize during the design of permanent magnet (PM) devices.

This parameter directly indicates the performance of the PM device design in terms of torque. The air-gap flux density is typically derived from simulations during the PM device design stage.

Flux density distribution in the air gap generally reveals the performance of torque ripple and the order of harmonics of the motor. The high-order harmonics will increase cogging torque and the eddy current loss.

Therefore, it is an inevitable metric while designing a PM device. The air gap flux density can commonly be represented in the polar coordinate system in 2D design or cylindrical coordinate system in 3D design to simplify the calculation process. It consists of two parts while ignoring the Z component, which can be expressed by

$$\begin{cases} B_\rho = B_x \cos(\phi) + B_y \sin(\phi) & (5) \\ B_\phi = -B_x \sin(\phi) + B_y \cos(\phi) & (6) \end{cases}$$

where B_x is x-component of the B vector, B_y is y-component of the B vector, B_ρ is radial-component of the B vector, B_ϕ is tangential-component of the B vector.

2) Magnetic Torque Calculation

Magnetic torque is one of the most critical performance indicators of magnetic gears. After determining the magnetic field distribution in the polar coordinate system in the two air gaps, the torque applied to the inner and outer rotors T_i and T_o can be obtained by using the Maxwell stress tensor [30], and is given by:

$$T_i = \frac{Lr_i^2}{\mu 0} \int_0^{2\pi} B_\rho(r_i, \theta) B_\theta(r_i, \theta) d\theta \tag{7}$$

$$T_o = \frac{Lr_o^2}{\mu 0} \int_0^{2\pi} B_\rho(r_o, \theta) B_\theta(r_o, \theta) d\theta \tag{8}$$

where L is the length of the model, r_i and r_o are the radius of the integration paths along the inner and outer air gaps, respectively.

III. GANs for Magnetic Field Approximation

In this section, a method capable of with the ability to addressing the introduced problem, namely, physics-informed GAN, is proposed. GAN is a machine learning framework designed by Goodfellow et al. in 2014 [26], i.e., two neural

networks compete in a zero-sum game, where the gains of one agent are the losses of the other agent.

A. Conditional GAN and Pix2Pix

Conditional GAN (cGAN) is one of GAN's earliest variants, changing the original GAN probabilities to conditional probabilities, i.e., cGANs learn a mapping from observed input x and random noise vector z, to y, $G: \{x, z\} \rightarrow y$. This condition can be pictures and annotations, making cGAN widely used in image processing and conversion.

Similar to GAN, the architecture of cGAN also consists of generator and discriminator models. The generator model can be responsible for generating new specious examples. Ideally, these examples are indistinguishable from the real examples in the dataset. The discriminator model is a classification network responsible for classifying a given input as ground-truth (extracted from the dataset) or fake (generated).

Pix2Pix is an efficient cGAN for image synthesis; it can effectively synthesize the output from labels, reconstruct objects from edge maps, and colorize images [27]. The objective function of Pix2Pix is defined as:

$$G^* = arg \min_G \max_D L_{cGAN}(G, D) + \lambda L_{L1}(G) \tag{9}$$

where $L_{cGAN}(G, D)$ is the loss function of PatchGAN, $L_{L1}(G)$ is the loss function of the generator (also is known as the mean absolute error (MAE)), and G^* is the final objective.

In our case, the generator network G is trained to generate the magnetic fields that match the material distribution of the input. The discriminator D is trained to determine whether the given inputs are constrained by the physical properties of magnetic fields.

B. Loss Functions for Magnetic Field Approximation

In Pix2Pix, the loss function of cGAN and L1 are:

$$L_{cGAN}(G, D) = E_{x,y}[\log D(x, y)] + E_{x,z}\left[\log\left(1 - D\left(x, G(x, z)\right)\right)\right] \tag{10}$$

$$L_{L1}(G) = E_{x,y,z}(||y - G(x, z)||) \tag{11}$$

where G tries to minimize this objective against an adversarial D that tries to maximize it.

For the Pix2Pix model, the generator not only fools the discriminator but also is near the ground-truth output in an L2 sense. Nevertheless, L1 distance is used rather than L2 as L1 encourages less blurring [27].

In magnetic field approximation, we have additional information on the underlying physics of magnetic fields. We not only want to generate a visually appealing result, but we also want the generated magnetic field can be used for the performance calculation of magnetic gears.

An existing research with excellent prediction ability employs a sum of square error (SSE) to measure the squared error between the predicted field and the results obtained by using FEM [22], which usually can be written as:

$$L_{SSE} = \sum (B_{NN} - B_{FEM})^2 \tag{12}$$

where B_{NN} and B_{FEM} are the calculated magnitude data by the neural network and the FEM at each point.

Moreover, since the torque is the critical parameter when analyzing magnetic gears, the torque can be obtained by the Maxwell stress tensor and given by (7) and (8). We can find the torque obtained by calculating the integral of radial component times tangential component of flux density. Therefore, minimizing the absolute error between the sum of the predicted magnetic field and the sum of the magnetic field obtained from FE simulation can be an effective method to find the solution.

The sum absolute error (SAE) of predicted results and FE simulation results is defined as:

$$L_{SAE} = \sum_{i=1}^{n} |B_{NN} - B_{FEM}| \tag{13}$$

where B_{NN} is the prediction, B_{FEM} is the results obtained from the FE simulation.

Our final loss function used during training is formulated as follows:

$$\mathrm{L} = L_{cGAN} + \lambda L_{SAE} \tag{14}$$

where L_{cGAN} is loss of discriminator and L_{SAE} is the loss of our generator, and λ is 1.

C. Neural Network Architecture

1) Generator

Two types of generators were implemented for the GANs in this work, and they are U-net and ResU-net

The U-net architecture does not have any fully connected layers, and they are replaced by upsampling operators that are added skip connections between each convolutional layer. An overview of this type of network is shown in Fig. 2, where the blue line represents the PM and iron inputs. Each blue box corresponds to a multi-channel feature map, and it includes a convolutional layer, a batch-normalization layer, and a ReLU activation. The number of channels is denoted on top of the box. The x–y size is provided at the lower-left edge of the box. The arrows denote the different operations.

The residual block was first introduced in residual networks (ResNets) [31]. It has demonstrated significant performance across many benchmarks in the computer vision field. Each residual block contains two convolution layers, two batch-normal layers, and two ReLU activations (c.f. Fig.2 (b)). The arrows denote the different operations.

ResU-net, a variant of U-net, combines the advantage of U-net and residual blocks [27]. It consists of a fine-to-coarse down-sampling path and a coarse-to-fine upsampling path with shortcut connections. Other network parameters are the same as the original U-net for every two convolutional layers at the same resolution level in U-net. The details of each block are

This article has been accepted for publication in IEEE Journal of Emerging and Selected Topics in Industrial Electronics. This is the author's version which has not been fully edited and content may change prior to final publication. Citation information: DOI 10.1109/JESTIE.2022.3185558

given in Fig. 2 (b). Both U-net and ResU-net were tested in our work with fine-tuning.

2) Discriminator

The overview of the discriminator network is shown in Fig. 3, where the blue line on the left represents the inputs, and the gray line represents the magnetic field data obtained from the FE simulation. This discriminator tries to classify if each M×N patch in an image is real or fake using a convolutional block and averages all responses to provide the ultimate output of D.

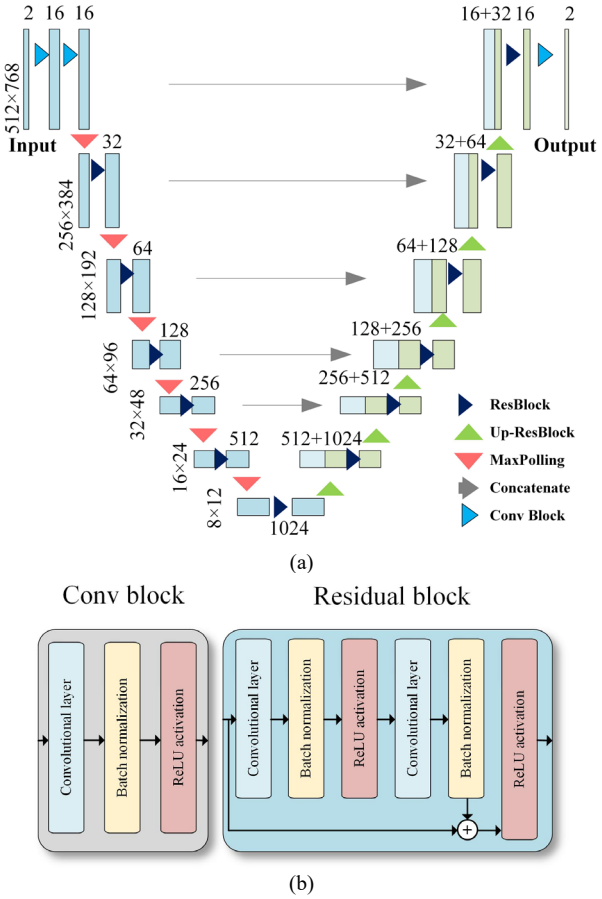

Fig. 2. The generator network. (a) ResU-net. (b) Details of blocks.

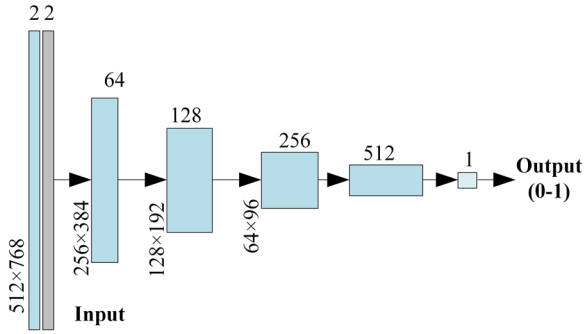

Fig. 3. The discriminator network.

IV. Performance Evaluation Using GAN Based Magnetic Field Approximation

This section presents the working principle and the training process of the proposed GAN model for magnetic field approximation in CMG.

A. Working Principle

Our model uses a ResU-net generator to approximate the magnetic field for CMG, see Fig 4. The detailed processes are described in the following:

Step 1: Material separation - the CMG model will be divided into two parts:

- Permeable materials – The relative permeability is greater than one and does not have a magnetization direction vector.
- Magnetic materials – The relative permeability is close to one and has a magnetization direction vector.

Step 2: Coordinate system (CS) conversion – we convert the input from the polar coordinate system into a rectangular coordinate system

Step 3: Pre-processing - we construct two tensors, namely the relative permeability tensor and the magnetization direction vector tensor. Then perform scaling and normalization operations on these two tensors, respectively. Then we do a padding operation on the preprocessed tensor to make its shape convenient for neural network model training and processing.

Step 4: Evaluation - Feeding the input of the data into the neural network model and obtaining the output.

Step 5: Inverse data manipulation - we slice the generator's output to obtain the shape before the padding operation for post-processing.

Step 6: Inverse coordinate system conversion – we utilize coordinate system conversion on the output, i.e., convert B_x, B_y to B_ρ, B_θ.

Step 7: Performance evaluation – we post-process the output to find the air gap magnetic density and torque.

In this way, users no longer need to learn how to use finite elements and prepare high-performance computers for performance evaluation, significantly reducing the user's learning threshold.

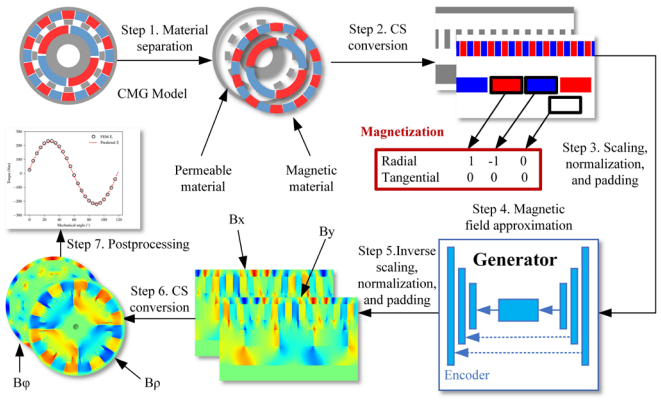

Fig 4. The workflow of magnetic field approximation for coaxial magnetic gears

B. Training Process

The detailed training process is demonstrated in Fig. 5. The FE simulation comes with a high computational cost but is executed only once. Moreover, the FE simulation can be

generated in parallel and with a distributed computing platform.

First, many FE simulations are done with different random combinations of the input variables. The output data are extracted from FE solutions.

In the second step, we assemble the dataset and implement data preprocessing from extracted solution data from the FE simulation. This process is described in the following:

1. Matrix scaling - The output is scaled concerning the magnitude of flux density, ranging from 0 to 3 Tesla.

2. Matrix normalization - All the input and output variables are normalized. In this study, we use min-max normalization.

$$x' = \frac{x - min(x)}{max(x) - min(x)} \tag{15}$$

3. Matrix padding – In the process of convolution, padding is sometimes needed to avoid information loss.

Afterward, the preprocessed dataset is used for the training of the cGAN. For cGAN, the generator should be saved, and it will be used to evaluate the magnetic field of CMG.

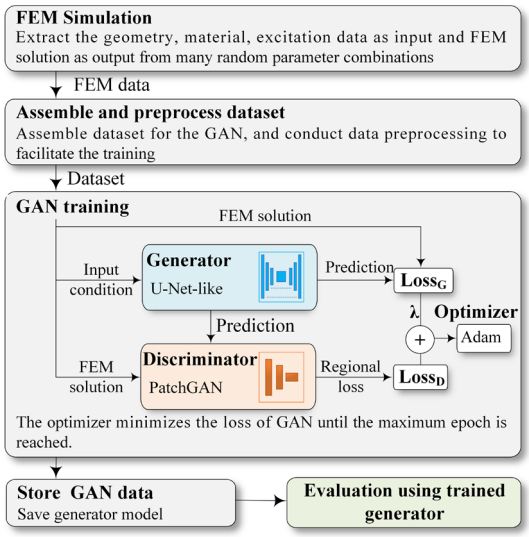

Fig. 5. The training process of magnetic field approximation for CMG using Pix2Pix.

C. Physical Property Representation

Magnetization of PM could influence the performance of CMG using FEM. In this study, we use a normalized vector to express the magnetization direction of the material. The first element of the vector represents the radial component, and the second element represents the tangential component. For example, (1, 0) indicates that the magnetizing direction is the positive radial direction, and (-1, 0) indicates that the magnetizing direction is the negative radial direction. (0,0) means non-magnetic material (cf. Fig 4).

D. Dataset Generation

Only the magneto-static problem is considered for a coaxial magnetic gear operating at low speed. The governing equation for the static magnetic field analysis, including a PM, is derived from Maxwell's equations as:

$$\nabla \times \left(\frac{1}{\mu_r \mu_0} \mathrm{B}\right) = 0 \tag{16}$$

$$\nabla \cdot B = 0 \tag{17}$$

$$\nabla \times H = J = 0 \tag{18}$$

$$B = \mu(H + M) \tag{19}$$

where μ_r denotes the relative magnetic permeability, μ_0 is the vacuum permeability (i.e., $4\pi \times 10^{-7} N/A^2$), B is the magnetic flux density, and B_r is the remanence of the PM material (i.e., the residual magnetic flux density), H stands for the magnetic field strength, M represents the magnetization strength of PM, and J represents the current density vector, which is determined as zero in this model. The parametric model of CMG is given in Fig. 6

The training dataset is used to train the parameters of the GAN model, and the testing dataset is used to check the performance of the cGAN model on the unseen data. The FE simulation results produced both the training and testing datasets.

The input tensor and output tensor of our Pix2Pix model have the exact size of 512×768 pixels. The tensor, including material distribution and PM magnetization, were interpolated from the results of the FE simulation with a spatial resolution of 0.1mm × 0.5 degree.

The magnetic field (B_x, B_y) are calculated in the 2-D FE simulation, then we use equation (5) and (6) to convert flux density B from Cartesian CS to Polar CS (c.f. Step 2 in Fig.5.).

The geometry parameters of the template CMG model are listed in Table I. Arbitrary pole pair of the high-speed and low-speed rotor, size of the yoke of the high-speed and low-speed rotor, and the open slot ratio of modulation iron segments and PM are simulated in the datasets. The rotor position was also randomly selected, as shown in Table II. The material of magnets is N35-NdFeB, the material of iron segments and two rotors is DW310, and the nonlinear B–H curve is shown in Fig. 7.

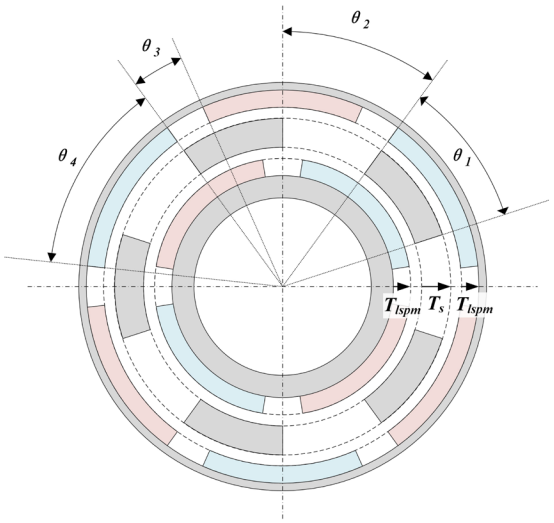

Fig. 6. The definition of the parametric CMG model.

We compute the resulting 2-D magnetic field and store 5,000 samples of these into the dataset, which is then used to train our neural networks. The hardware list of the training workstation is given in Table III.

TABLE I
LIST OF FIXED PARAMETERS OF THE CMGS

	Parameter	Value	Unit
R_o	Outside radius of the MG	92	mm
T_{lspm}	The thickness of the PMs on the low-speed rotor	7.8	mm
T_{hspm}	The thickness of the PMs on the high-speed rotor	7.8	mm
T_s	The thickness of the modulation iron segments	13	mm
g	The length of the air gap	0.6	mm
L	Stack length	40	mm

TABLE II
LIST OF VARIABLES OF THE CMGS

	Parameter	Min.	Max.	Unit
P_{hs}	Number of pole-pairs at HS rotor	3	5	-
P_{ls}	Number of pole-pairs at HS rotor	10	25	-
N_s	Number of modulation iron segments	10	25	-
T_{oy}	The thickness of the yoke of the outer rotor	5	10	mm
T_{iy}	The thickness of the yoke of the inner rotor	5	10	mm
Ra_i	Slot open of modulation iron segments = $\theta_1/(\theta_1+\theta_2)$	0.3	0.7	-
Ra_{pm}	Ratio PM = $\theta_3/(\theta_3+\theta_4)$	0.5	1	-
φ_{ls}	Low-speed rotor position	0	360	Deg.

TABLE III
HARDWARE LIST FOR MAGNETIC FIELD APPROXIMATION

Hardware	Model	Specification
CPU	Intel Core i7-10870H	8-core @ 2.2GHz
GPU	NVIDIA GeForce RTX 3080 M	16GB RAM
RAM	DDR4 3200MHz	64GB

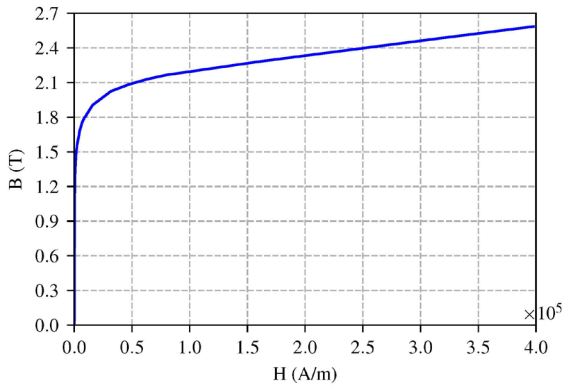

Fig. 7. The B-H curve of steel DW310 in the modulation iron segment and two rotors.

V. INFLUENCE OF KEY PARAMETERS OF PROPOSED FAST MAGNETIC APPROXIMATION METHOD

In order to discover the relationships between the key parameters and performances of magnetic field approximation, the influences that key parameters have on the network are investigated in this section. Except for specifically indicated parameters, design parameters of the CMG are fixed as given in Table I in the investigation of the influence of critical parameters.

In our network, the stochastic gradient-based optimization algorithm, Adam [32], is used. The learning rate value determined was 2×10^{-4}. The proposed model is implemented in Python 3 environment with TensorFlow [33].

In order to objectively demonstrate the superiority of the proposed method, all the experiments were quantitatively evaluated using the structural similarity (SSIM) index and the peak signal-to-noise ratio (PSNR). The SSIM index measures the similarity of structural information in two images, where 0 indicates no similarity and 1 indicates total positive similarity. PSNR measures image distortion and noise level between two images. A higher PSNR value indicates a higher image quality. SSIM and PSNR are used for similarity verification of magnetic fields [34].

A. Layer Type of Generator

ResU-net is a fully convolutional neural network designed to get high performance with fewer parameters. It is an improvement over the existing U-net architecture. ResU-net takes advantage of both the U-net architecture and the deep residual learning.

The ResU-net consists of an encoding network, decoding network, and a bridge connecting these networks, just like a U-net. The U-net uses two 3 × 3 convolutions, where a ReLU activation function follows each. In the case of ResU-net, these layers are replaced by a pre-activated residual block.

B. MAE and SAE combined with λ

Since the difference between MAE and SAE is the number n of elements used for the computation, a comparison between SAE and MAE used for generators in Pix2Pix is conducted. For SAE, equivalent λ (i.e., 512×768 = 393,216) is used in comparison. Also, we investigate the relationship between the indicators and the value of λ ranging from 1 to 10^8.

C. Quantitative evaluation

U-net and ResU-net are implemented by employing two different kinds of loss functions. Table IV presents the performance on average MAE, SSIM, and PSNR across each method. It can be seen that the ResU-net combined with SAE demonstrates superior performance in cases compared to U-net, indicating that ResU-net works better along with the SAE in this work.

It is observed that the value λ between 10^4 and 10^6 has better performance than other values under the same generators, in which Pix2Pix with equivalent λ value at 786,432 (512×768×2) has achieved the best MAE, PSNR, and SSIM.

This article has been accepted for publication in IEEE Journal of Emerging and Selected Topics in Industrial Electronics. This is the author's version which has not been fully edited and content may change prior to final publication. Citation information: DOI 10.1109/JESTIE.2022.3185558

TABLE IV
COMPARISON OF METRICS WITH DIFFERENT GENERATORS

Generator	Loss	λ	MAE ($\times 10^{-3}$) ↓	SSIM ↑	PSNR ↑
U-net	MAE [a]	100	19.90	0.8964	29.45
	SAE	1[b]	7.39	0.9811	39.23
ResU-net	MAE	100	13.39	0.9311	30.01
	SAE	**1[b]**	**2.62**	**0.9962**	**47.42**
ResU-net	MAE	10^0	75.67	0.7526	18.91
		10^1	85.16	0.7124	18.15
		10^2	12.73	0.9422	30.89
		10^3	6.46	0.9712	32.16
		10^4	3.55	0.9942	43.95
		10^5	2.91	0.9954	46.83
		10^6	3.59	0.9941	44.87
		10^7	3.66	0.9956	45.88
		10^8	3.65	0.9952	45.74

MAE, SSIM, and PSNR are calculated based on the mean value of the whole dataset. The arrow " ↓ " means lower is better, and " ↑ " means higher is better.

[a]U-net+MAE is the original configuration of the generator in Pix2Pix.

[b]The equivalent value of λ using MAE is 786,432 (512×768×2), which is between 10^5 and 10^6.

VI. EXPERIMENTAL VERIFICATION

In the following section, we evaluate our novel method for magnetic field approximation and calculate the performance of CMG. In order to validate the proposed model, the predicted results have been compared with 2-D FE simulations obtained using ANSYS Maxwell software. The geometrical parameters given in Table V are considered.

The training of our final model takes 76 hours. As for the evaluation process, the total magnetic field approximation time of the 360-step CMG model using our model is 26 seconds, of which the total neural network evaluation takes 11.65 seconds (the first step takes 4.4 seconds for initialization), the file read takes 10.55 seconds, and the torque calculation takes 0.44 seconds, the remaining time was used for preprocessing and postprocessing. In comparison, the conventional FE simulation takes 26 minutes, and each step takes 4 seconds on average. Convergence is achieved in around 800k to 1000k iterations depending on the network configuration, as is shown in Fig.8.

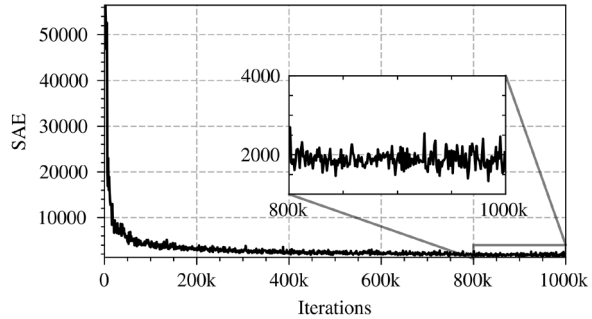

Fig. 8. Overview of SAE after 1000k-iteration training. The generator is the ResU-net, combined with SAE as the loss function.

TABLE V
LIST OF FIXED PARAMETERS OF THE CMGS

	Parameter	Value	Unit
R_o	Outside radius of the MG	92	mm
T_{lspm}	The thickness of the PMs on the low-speed rotor	7.8	mm
T_{hspm}	The thickness of the PMs on the high-speed rotor	7.8	mm
T_s	The thickness of the modulation iron segments	13	mm
g	The length of the air gap	0.6	mm
L	Stack length	40	mm
P_{hs}	Number of pole-pairs at HS rotor	3	-
P_{ls}	Number of pole-pairs at HS rotor	22	-
N_s	Number of modulation iron segments	25	-
T_{oy}	The thickness of the yoke of the outer rotor	10	mm
T_{iy}	The thickness of the yoke of the inner rotor	3.4	mm
Ra_i	Slot open of modulation iron segment = $\theta_1/(\theta_1+\theta_2)$	0.5	-
Ra_{pm}	Ratio PM = $\theta_3/(\theta_3+\theta_4)$	0.9	-

A. Flux Density Distribution

Our model has been tested using a CMG with the parameters listed in Table V. Fig. 9 shows the results of predicting the magnetic field of a specific magnetic gear after using various combinations of loss functions and network structures. It can be observed that almost all the predictions are similar to the FEM solution, and the errors are hard to find visually as the mean absolute percentage error of each is less than 1%.

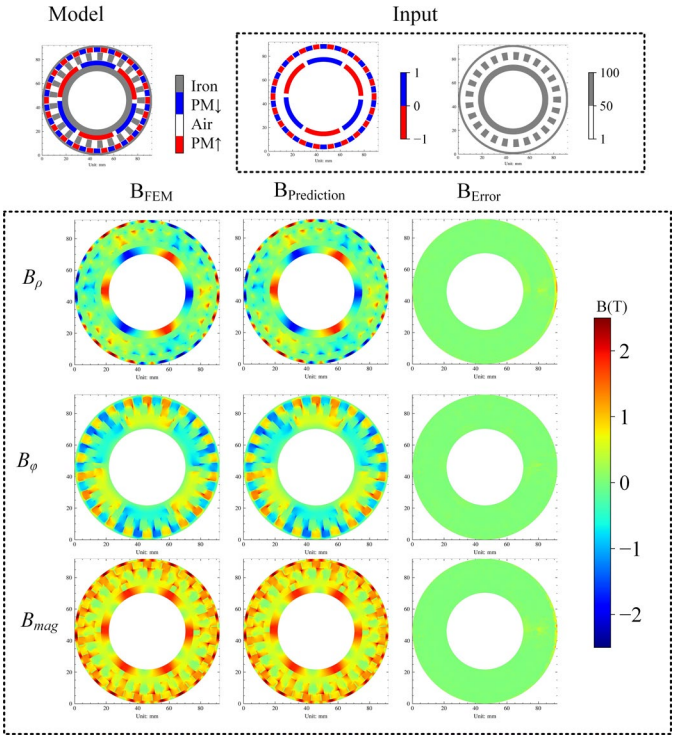

Fig. 9. Qualitative analysis on magnetic field prediction in the experimental 2-D setup with a generator network. The input and the predicted magnetic field of B_ρ, B_ϕ and B_{mag} are presented. Visually, our method achieves to reconstruct the magnetic field obtained by FE simulation almost perfectly.

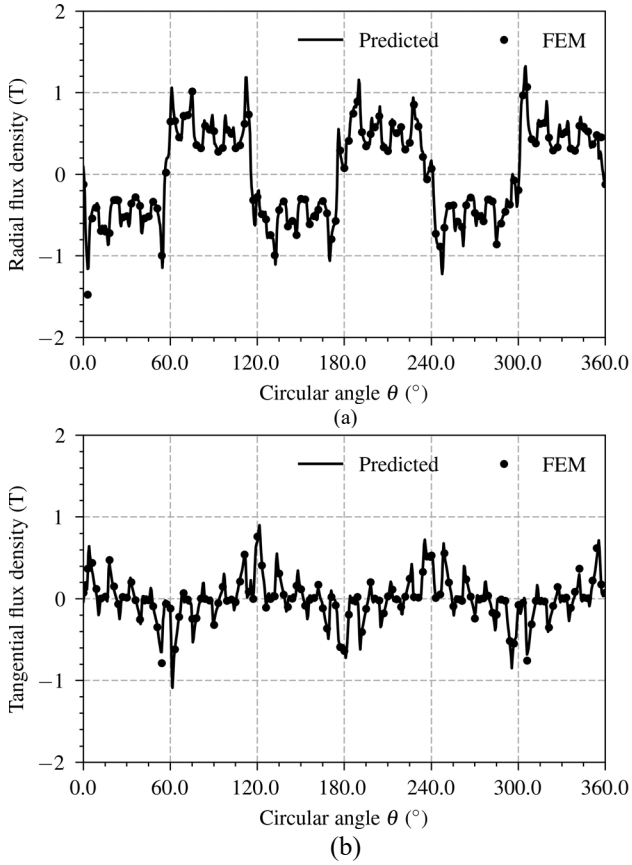

Fig. 10. Flux density distribution in the middle of the inner air gap (r = 66.9mm): (a) radial component and (b) tangential component.

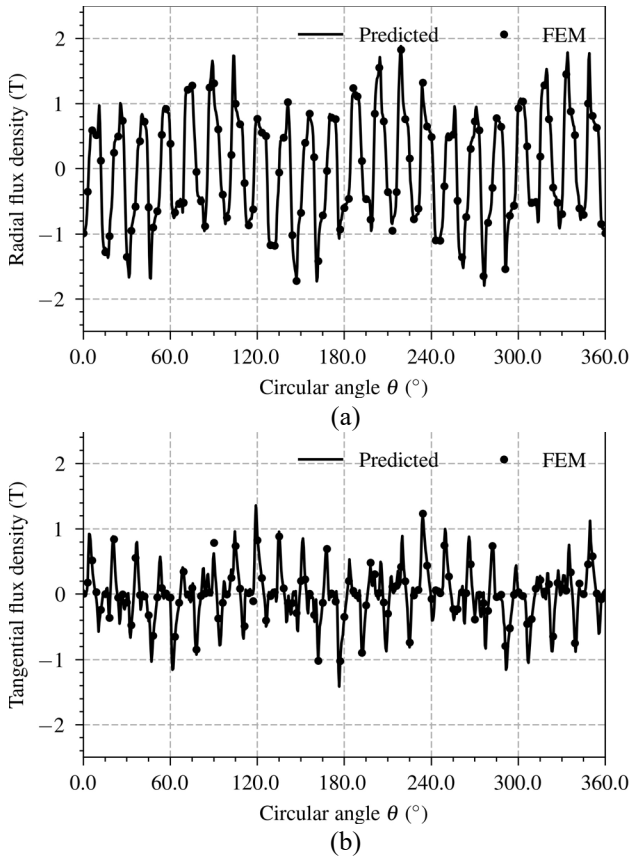

Fig. 11. Flux density distribution in the middle of the outer air gap (r = 80.5mm): (a) radial component and (b) tangential component.

The corresponding flux density distributions (radial and tangential components) in the middle of the inner air gap (r = 66.9mm) and in the middle of the outer air gap (r = 80.5mm) are plotted, respectively. Fig. 10 (a) and Fig. 10 (b) show the radial and tangential components of the magnetic flux density in the inner air gap of CMG. Furthermore, the radial and tangential components of the flux density distribution in the middle of the outer air gap are shown in Fig. 11 (a) and Fig. 11 (b). We can observe a very good agreement between the results predicted by our model and the results obtained from FE simulation for both radial and tangential components.

B. Torque

Fig. 12 shows the torque variation exerted on the inner rotor while keeping the pole-pieces ring and the outer rotor fixed. The inner rotor rotates with a phase angle varying from 0 to 120 degrees. The predicted results are in good agreement with those obtained by the FEM.

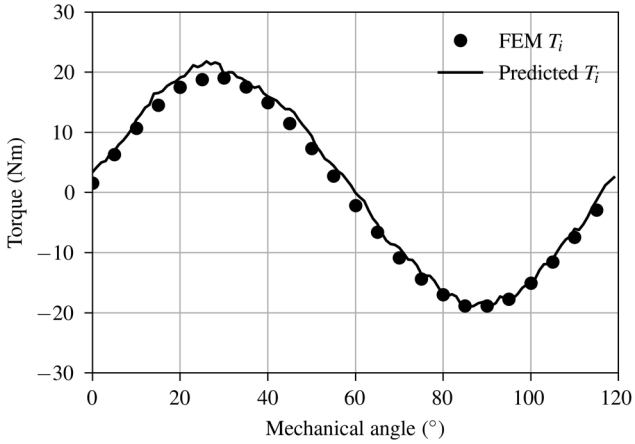

Fig. 12. The torque–angle curve predicted by our model (ResU-net as the generator, combined with SAE as the loss function).

VII. Conclusion

This paper proposes a fast magnetic field approximation method for CMGs using cGAN. Based on the magnetic field approximation technique in the 2D polar coordinate system, the flux density and torque for a magnetic field produced by PMs in CMGs have been presented.

The empirical analyses showed that the cGAN model could approximate the magnetic fields for CMGs accurately, and its generalization ability is excellent, which allows various combination of pole-pairs. The predicted magnetic torque obtained by the air gap flux density and Maxwell tensor method is consistent with the FE simulation results.

In addition to improved predictive performance, our model required a significantly lower model prediction time, making neural networks a more practical approach for adoption in optimization processes.

We note that our model performs excellent magnetic field approximation within the design space. The proposed cGAN model-based performance evaluation method can be advantageous in the real-time magnetic field approximation for optimal design of electric machines.

ACKNOWLEDGMENTS

This work was supported by the National Natural Science F oundation of China under Project 52077187 and in part by the Research Grant Council of the Hong Kong Government under Project PolyU 152143/18E and PolyU 152109/20E.

REFERENCES

[1] D. Fodorean, "State of the Art of Magnetic Gears, their Design, and Characteristics with Respect to EV Application," *Model. Simul. Electr. Veh. Appl.*, vol. 3, 2016, doi: 10.5772/64174.

[2] K. H. Shin, H. Il Park, H. W. Cho, and J. Y. Choi, "Parametric analysis and optimized torque characteristics of a coaxial magnetic gear based on the subdomain analytical model," *AIP Adv.*, vol. 7, no. 5, 2017, doi: 10.1063/1.4973798.

[3] A. Al-Qarni, F. Wu, and A. Ei-Refaie, "High-torque-density low-cost magnetic gear utilizing hybrid magnets and advanced materials," *2019 IEEE Int. Electr. Mach. Drives Conf. IEMDC 2019*, no. i, pp. 225–232, 2019, doi: 10.1109/IEMDC.2019.8785338.

[4] X. Zhao and S. Niu, "Design and Optimization of a New Magnetic-Geared Pole-Changing Hybrid Excitation Machine," *IEEE Trans. Ind. Electron.*, vol. 64, no. 12, pp. 9943–9952, 2017, doi: 10.1109/TIE.2017.2716879.

[5] T. V. Frandsen *et al.*, "Motor Integrated Permanent Magnet Gear in a Battery Electrical Vehicle," *IEEE Trans. Ind. Appl.*, vol. 51, no. 2, pp. 1516–1525, 2015, doi: 10.1109/TIA.2014.2360016.

[6] N. W. Frank, S. Pakdelian, and H. A. Toliyat, "A magnetic gear with passive transient suppression capability," *2011 IEEE Electr. Sh. Technol. Symp. ESTS 2011*, no. c, pp. 326–329, 2011, doi: 10.1109/ESTS.2011.5770891.

[7] N. W. Frank and H. A. Toliyat, "Gearing ratios of a magnetic gear for marine applications," *IEEE Electr. Sh. Technol. Symp. ESTS 2009*, pp. 477–481, 2009, doi: 10.1109/ESTS.2009.4906554.

[8] J. J. Scheidler, V. M. Asnani, and T. F. Tallerico, "NASA's Magnetic Gearing Research for Electrified Aircraft Propulsion," *2018 AIAA/IEEE Electr. Aircr. Technol. Symp. EATS 2018*, pp. 1–12, 2018, doi: 10.2514/6.2018-4988.

[9] H. Y. Wong, J. Z. Bird, D. Barnett, and W. Williams, "A high torque density halbach rotor coaxial magnetic gear," *2019 IEEE Int. Electr. Mach. Drives Conf. IEMDC 2019*, pp. 233–239, 2019, doi: 10.1109/IEMDC.2019.8785188.

[10] X. Liu and H. Wang, "Analytical calculation and analysis of air gap magnetic field for electromechanical integrated toroidal drive," *Adv. Mech. Eng.*, vol. 11, no. 12, pp. 1–13, 2019, doi: 10.1177/1687814019895925.

[11] T. Lubin, S. Mezani, and A. Rezzoug, "Analytical computation of the magnetic field distribution in a magnetic gear," *IEEE Trans. Magn.*, vol. 46, no. 7, pp. 2611–2621, 2010, doi: 10.1109/TMAG.2010.2044187.

[12] Y. C. Wu and B. S. Jian, "Magnetic field analysis of a coaxial magnetic gear mechanism by two-dimensional equivalent magnetic circuit network method and finite-element method," *Appl. Math. Model.*, vol. 39, no. 19, pp. 5746–5758, 2015, doi: 10.1016/j.apm.2014.11.058.

[13] X. Zhang, X. Liu, C. Wang, and Z. Chen, "Analysis and design optimization of a coaxial surface-mounted permanent-magnet magnetic gear," *Energies*, vol. 7, no. 12, pp. 8535–8553, 2014, doi: 10.3390/en7128535.

[14] N. Misron, L. M. Saini, I. Aris, C. A. Vaithilingam, and H. Tsuyoshi, "Simplified design of magnetic gear by considering the maximum transmission torque line," *Appl. Sci.*, vol. 10, no. 23, pp. 1–14, 2020, doi: 10.3390/app10238581.

[15] X. Yin, P. Pfister, and Y. Fang, "A novel magnetic gear: Towards a higher torque density," *2015 IEEE Int. Magn. Conf. INTERMAG 2015*, no. 2013, p. 4095, 2015, doi: 10.1109/INTMAG.2015.7157676.

[16] A. Khan, V. Ghorbanian, and D. Lowther, "Deep learning for magnetic field estimation," *IEEE Trans. Magn.*, vol. 55, no. 6, pp. 1–4, 2019, doi: 10.1109/TMAG.2019.2899304.

[17] S. L. Brunton, M. Budišić, E. Kaiser, and J. N. Kutz, "Modern Koopman Theory for Dynamical Systems," 2021, [Online]. Available: http://arxiv.org/abs/2102.12086

[18] A. Essien and C. Giannetti, "A Deep Learning Model for Smart Manufacturing Using Convolutional LSTM Neural Network Autoencoders," *IEEE Trans. Ind. Informatics*, vol. 16, no. 9, pp. 6069–6078, 2020, doi: 10.1109/TII.2020.2967556.

[19] B. Lusch, J. N. Kutz, and S. L. Brunton, "Deep learning for universal linear embeddings of nonlinear dynamics," *Nat. Commun.*, vol. 9, no. 1, 2018, doi: 10.1038/s41467-018-07210-0.

[20] M. H. Mohammadi, V. Ghorbanian, and D. A. Lowther, "A Data-Driven Approach for Design Knowledge Extraction of Synchronous Reluctance Machines Using Multi-Physical Analysis," *Proc. - 2018 23rd Int. Conf. Electr. Mach. ICEM 2018*, pp. 479–485, 2018, doi: 10.1109/ICELMACH.2018.8506851.

[21] D. Kochkov, J. A. Smith, A. Alieva, Q. Wang, M. P. Brenner, and S. Hoyer, "Machine learning – accelerated computational fluid dynamics," 2021, doi: 10.1073/pnas.2101784118/-/DCSupplemental.y.

[22] S. Qi, Y. Wang, Y. Li, X. Wu, Q. Ren, and Y. Ren, "Two-Dimensional Electromagnetic Solver Based on Deep Learning Technique," *IEEE J. Multiscale Multiphysics Comput. Tech.*, vol. 5, pp. 83–88, 2020, doi: 10.1109/JMMCT.2020.2995811.

[23] R. Gong and Z. Tang, "Training Sample Selection Strategy applied to CNN in Magneto-Thermal coupled Analysis," *IEEE Trans. Magn.*, vol. 9464, no. c, pp. 8–11, 2021, doi: 10.1109/TMAG.2021.3058131.

[24] S. Pollok, R. Bjork, and P. S. Jorgensen, "Inverse Design of Magnetic Fields using Deep Learning," *IEEE Trans. Magn.*, 2021, doi: 10.1109/TMAG.2021.3082431.

[25] S. Doi, H. Sasaki, and H. Igarashi, "Multi-objective topology optimization of rotating machines using deep learning," *IEEE Trans. Magn.*, vol. 55, no. 6, pp. 1–5, 2019, doi: 10.1109/TMAG.2019.2899934.

[26] I. Goodfellow *et al.*, "Generative adversarial networks," *Commun. ACM*, vol. 63, no. 11, pp. 139–144, Jun. 2020, doi: 10.1145/3422622.

[27] P. Isola, J. Y. Zhu, T. Zhou, and A. A. Efros, "Image-to-image translation with conditional adversarial networks," *Proc. - 30th IEEE Conf. Comput. Vis. Pattern Recognition, CVPR 2017*, vol. 2017-Janua, pp. 5967–5976, 2017, doi: 10.1109/CVPR.2017.632.

[28] S. Arora, R. Ge, Y. Liang, T. Ma, and Y. Zhang, "Generalization and equilibrium in generative adversarial nets (GANs)," *34th Int. Conf. Mach. Learn. ICML 2017*, vol. 1, pp. 322–349, 2017.

[29] K. Atallah and D. Howe, "A novel high-performance magnetic gear," *IEEE Trans. Magn.*, vol. 37, no. 4 I, pp. 2844–2846, Jul. 2001, doi: 10.1109/20.951324.

[30] B. Praslicka, M. C. Gardner, M. Johnson, and H. A. Toliyat, "Review and Analysis of Coaxial Magnetic Gear Pole Pair Count Selection Effects," *IEEE J. Emerg. Sel. Top. Power Electron.*, vol. 10, no. 2, pp. 1813–1822, 2021, doi: 10.1109/JESTPE.2021.3053544.

[31] K. He, X. Zhang, S. Ren, and J. Sun, "Deep residual learning for image recognition," *Proc. IEEE Comput. Soc. Conf. Comput. Vis. Pattern Recognit.*, vol. 2016-Decem, pp. 770–778, 2016, doi: 10.1109/CVPR.2016.90.

[32] D. P. Kingma and J. L. Ba, "Adam: A method for stochastic optimization," *3rd Int. Conf. Learn. Represent. ICLR 2015 - Conf. Track Proc.*, pp. 1–15, 2015.

[33] M. Abadi *et al.*, "TensorFlow: A system for large-scale machine learning," 2016.

[34] M. Le, C. T. Pham, and J. Lee, "Deep neural network for simulation of magnetic flux leakage testing," *Meas. J. Int. Meas. Confed.*, vol. 170, no. November, p. 108726, 2021, doi: 10.1016/j.measurement.2020.108726.